IEEE Journal of Microwaves

Received 22 April 2024; revised 24 June 2024; accepted 24 June 2024.

Digital Object Identifier 10.1109/JMW.2024.3419430

A 79 GHz SiGe Doherty Power Amplifier Suitable for Next-Generation Automotive Radar

JAN SCHOEPFEL (Member, IEEE), TOBIAS T. BRAUN (Graduate Student Member, IEEE), JULIA HELLWIG, HOLGER RÜCKER, AND NILS POHL (Senior Member, IEEE)

(Regular Paper)

[1]Institute of Integrated Systems, Ruhr-University Bochum, 44801 Bochum, Germany
[2]IHP- Leibniz-Institut für innovative Mikroelektronik, 15236 Frankfurt (Oder), Germany
[3]Fraunhofer Institute for High Frequency Physics and Radar Techniques (FHR), 53343 Wachtberg, Germany

CORRESPONDING AUTHOR: Jan Schoepfel (email: jan.schoepfel@rub.de).

This work was supported by the Federal Ministry of Education and Research, Berlin, Germany, within the Research Project VERANO under Grant 16ME0793.

ABSTRACT The number of environment-detecting sensors inside cars continuously increases, to enable failsafe autonomous driving. With more sensors, the probability of performance degrading interferences increases. A promising solution to the interferences is orthogonal frequency division multiplex (OFDM) radar. Due to the complex modulation scheme, the analog front end, especially the power amplifier in the transmitter, has to deal with a high peak-to-average power ratio. Therefore, conventional amplifiers have to be operated in power back-off to maintain linear operation at the drawback of reduced power-added efficiency. To mitigate this problem, a Doherty power amplifier for an automotive radar transceiver is proposed. In this work, we present a design methodology for an integrated Doherty amplifier for automotive radar applications, focussing on the theory of operation by analyzing transistor-level simulations. Small- and large signal simulations analyze the concept of load modulation for a Doherty amplifier in the automotive frequency band from 76–81 GHz. Using a fully differential transmission-line-based approach, we showcase the superior performance of an automotive Doherty amplifier over an conventional state-of-the-art reference amplifier. In measurements, the proposed Doherty amplifier achieves a saturated output power of 17.2 dBm with a peak power-added efficiency of 11.6%. When operating in 6 dB back-off, the PAE still amounts to 6.1%. Thereby we propose to improve conventional automotive power amplifiers by incorporating them into a Doherty amplifier.

INDEX TERMS Doherty, power amplifier, automotive, W-Band, millimeter-wave (mm-wave), monolithic microwave integrated circuit (MMIC), SiGe.

I. INTRODUCTION

Fully autonomous driving is one of the most promising technological solutions to the challenges of modern personal transportation. Therefore, environment detecting sensors that operate robustly for any weather and lighting condition are required. Radar sensors are robust for a wide range of scenarios, so they are an excellent choice for autonomous driving.

For advanced driver assistance systems like adaptive cruise control, long-range radar is already used in the mass market. These sensors are based on the frequency-modulated continuous wave (FMCW) concept, as it allows for precise detection of range and relative velocity [1]. For long-range scenarios such as highway driving, these FMCW radar sensors are perfectly suitable as the number of targets that has to be detected is small. In addition, these targets are spacially mainly limited to a small angular range in the direction of travel, which can be scanned with a small number of radar sensors. However, when considering dense urban traffic scenarios, the requirements of the sensors change.

In particular, the number of targets at close range to the sensor dramatically increases resulting in a significantly increased angular range the sensor has to cover. Multiple input

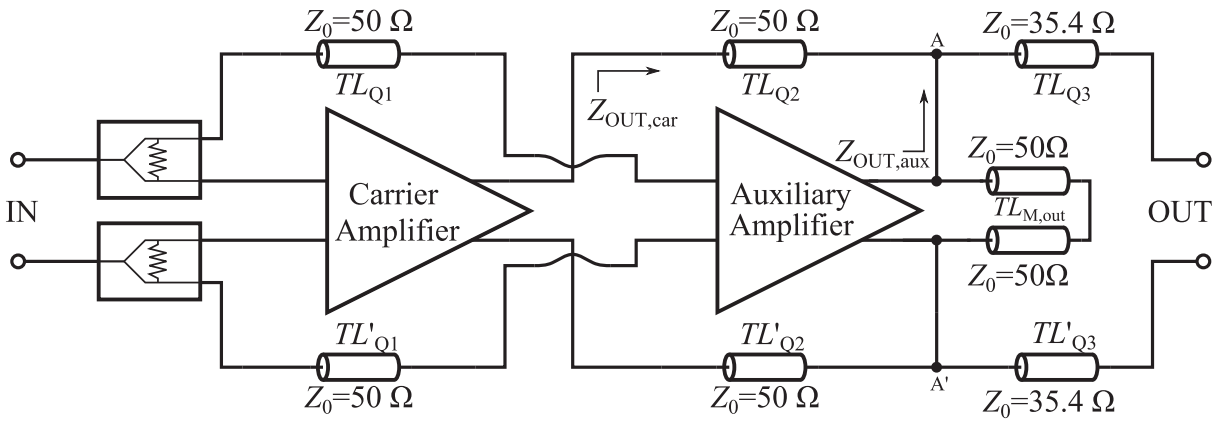

FIGURE 1. **Block diagram of the proposed differential Doherty amplifier. The load modulation networks are realized with transmission lines to achieve a fully differential design while being able to adapt the network through cutting laser fuses after manufacturing.**

multiple output (MIMO) radar sensors, which consist of multiple transmit and receive channels, are capable of covering the increased angular range and thus enable angle-resolved distance measurement. Furthermore, in a dense urban scenario, the number of vehicles that are also equipped with radar is significantly higher, which increases the probability of mutual interference between individual radar sensors and can lead to the detection of ghost targets [2]. An approach to improve the sensor's robustness against interference is to use orthogonality in the modulation schemes of the sensors. Since those challenges have successfully been addressed by the use of orthogonal frequency division multiplexing (OFDM) in mobile communications, utilizing the same modulation scheme in automotive radar is an ongoing research topic both in signal processing and hardware realization. Unlike for FMCW based radar, complex modulation schemes like OFDM require a software-defined-radio-based hardware platform [3], [4], [5]. One of the key components in such a platform is the power amplifier (PA) as it has to handle a high peak-to-average power ratios (PAPRs) originating from the large number of orthogonal subcarriers inside an OFDM symbol. Therefore, in contrast to an FMCW radar, the power amplifier cannot be operated in saturation, where it simultaneously offers the highest output power and efficiency. To ensure a linear amplification of OFDM signals, the power amplifier has to be operated in power back-off (PBO) from the compression. Thus reducing its power-added efficiency (PAE) and the radar's signal-to-noise ratio (SNR) due to the lower output power. However, since those drawbacks also affect mobile communications, several approaches have been introduced in that field of research. On the one hand, techniques like selected mapping or tone reservation can be used to initially reduce the PAPR [6]. However, these methods have several drawbacks, like increasing the bit error rate (BER), data rate, or computational complexity. On the other hand, there are several hardware-related approaches to deal with distortions caused by a high PAPR.

Besides envelope tracking or outphasing techniques like the Chireix amplifier [7], [8], the Doherty amplifier is one of the most commonly used approaches to increase the PAE in the PBO. The Doherty architecture originates from tube-based radio transmitters in the 1930s [9] to cope with enormous power consumption, reduce operating costs and improve device lifetime and reliability. With the transition towards solid-state circuits and more complex modulations getting popular, the Doherty amplifier became an attractive solution for cellular base stations [10]. Due to the advent of digital modulation in automotive radar, the Doherty amplifier represents a promising architecture for the next generation of automotive radar sensors. In recent years several publications have shown Doherty designs for increasingly higher frequencies reaching up to 130 GHz, proving an increased PAE in the PBO [11], [12], [13]. However, the state-of-the-art power amplifiers for automotive radar sensors are often realized as conventional differential amplifiers operated in the class-A regime. Therefore we propose a design methodology for a transmission-line-based Doherty amplifier for automotive OFDM radar that incorporates a conventional class-A carrier amplifier, which stands substitutionally for conventional state-of-the-art automotive amplifiers. This methodology offers a practicable design concept to improve conventional automotive power amplifiers in terms of PBO performance, linearity, and output power. Thereby we showcase the Doherty architecture as a promising solution improving the hardware platform for automotive OFDM radar in terms of efficiency and output power.

We recently published a brief overview of the proposed Doherty amplifier, containing the basic circuit concepts and first small- and large-signal measurements [14]. This article is an extended version, expanding the information on all circuit components. Especially the load modulation is considered in more detail and supported by theory and simulations. Furthermore, linearity investigations extend this article. Therein, the performed measurements of the error vector magnitude (EVM) highlight the concept's suitability for OFDM radar

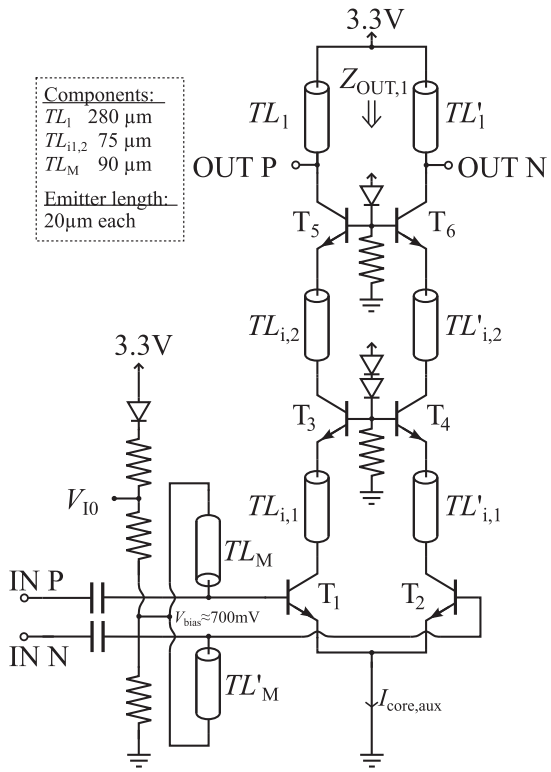

FIGURE 2. Schematic of the proposed auxiliary amplifier consisting of a common-emitter amplifier and two stacked common base stages.

systems by improving upon the carrier amplifier's output power and PAE at the same EVM.

This article is therefore organized as follows: Section II describes the functioning principle of the proposed Doherty amplifier and highlights the key components and design parameters, which will be especially important for mmWave frequencies. Furthermore, the design flow of the proposed amplifier is examined in simulation. Measurement results of the Doherty amplifier are shown in Section III. Finally, conclusions are drawn in Section IV.

II. ARCHITECTURE AND SIMULATIONS

The Doherty architecture consists of two separate amplifier circuits, as depicted in the block diagram of the proposed amplifier in Fig. 1. As the carrier amplifier is the main amplifying component, it is biased in class-A regime and thus operates for any input signal level. The second amplifier, which is connected in parallel, offers an inputpower-dependent amplification characteristic. For low input powers, when the carrier amplifier operates linearly, the auxiliary amplifier is designed to be inactive. When the carrier amplifier is driven into saturation, the auxiliary amplifier starts to contribute current to the shared load, lowering the impedance seen from the output of the carrier amplifier. The load-modulating network that connects the outputs of the carrier and the auxiliary amplifier ensures that for low input powers, the auxiliary amplifier is seen as a high impedance and does not contribute to the load.

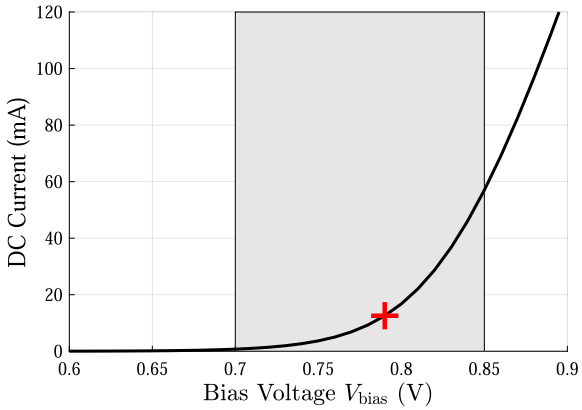

FIGURE 3. Simulated collector current in dependency of the base potential at a temperature of 80 °C. Operating the transistor in the marked region, the characteristic of the collector current can be used to realize the auxiliary amplifier, as shown in Fig. 2. The specific operation point is also marked.

Therefore the carrier amplifier sees an output impedance of $2R$ for low input powers. The output impedance seen by the carrier amplifier reduces to R for increasingly higher input powers as the auxiliary amplifier turns on and modulates the impedance. This load modulation shifts the compression point towards a higher power level and increases the PAE in back-off.

A. AUXILIARY AMPLIFIER

The Doherty amplifier demands an input-power-dependent amplification characteristic inside the auxiliary amplifier to realize the load modulation. Therefore, the circuitry of the proposed auxiliary amplifier is shown in Fig. 2. This amplifier is biased in class-C operation. Therefore a current-mirror-based current source can not be used, as it forces the amplifier to class-A operation. Instead, the amplifier consists of a quasi differential common emitter circuit with two stacked common base stages. The emitters of the common emitter stage are directly connected to ground. A resistive divider connects to the bases of T_1 and T_2 to adjust the base potential and, thereby, the base-emitter-voltage V_{BE}. Therefore the base potential of T_1 and T_2 adjusts the bias point of this circuitry.

Biasing the transistors T_1 and T_2 in the region marked gray in Fig. 3 ensures that the core current $I_{core,aux}$ of the auxiliary amplifier remains insignificant for low input amplitudes. For increasing input amplitude, $I_{core,aux}$ rises. This results in an increased DC current consumption and, therefore, amplifying characteristic dependent on the input power P_{in}:

$$G_P = \begin{cases} < 0\ \text{dB}, & P_{in} < P_{in,TO} \\ \geq 0\ \text{dB} & P_{in} \geq P_{in,TO} \end{cases} \quad (1)$$

For input powers below the turn-on-point $P_{in,TO}$, the amplifier stays inactive and offers a power gain G_P below 0 dB. Above an input power of $P_{in,TO}$, the DC current consumption of the auxiliary amplifier increases up to 75 mA, resulting in a significant power gain. Biasing the bases of T_1 and T_2 at a

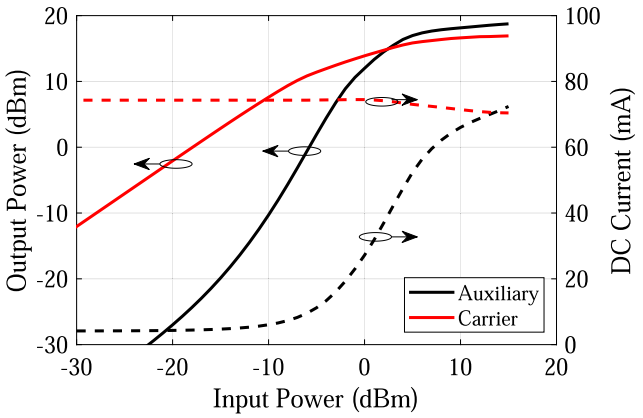

FIGURE 4. Output power characteristic of the proposed auxiliary amplifier and the carrier amplifier. Based on the simulation, $P_{\text{in,TO}}$ is designed to be approximately −10 dBm. Due to the exponential characteristic of the auxiliary amplifier the amplifier's DC current consumption is input-power-dependent.

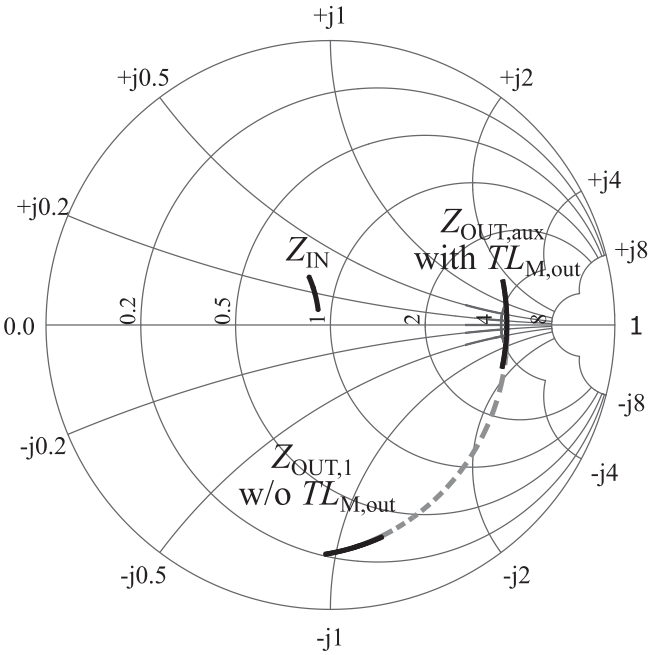

FIGURE 5. Smith chart, normalized to differential 100 Ω, showing the input and output impedance of the proposed auxiliary amplifier. The input impedance is near 100 Ω and therefore offers a good match. By using the transmission line $TL_{\text{M,out}}$ at the amplifier's output, the output impedance gets transformed into a real impedance of 400 Ω.

bias voltage of approximately 700 mV results in a simulated output power characteristic shown in Fig. 4. In the small signal regime, well below $P_{\text{in,TO}}$, the power gain amounts to −9 dB. In the active region, the amplifier offers a gain of up to 10 dB and saturated output power of 18 dBm. Beside the auxiliary amplifier's behaviour the characteristic of the proposed carrier amplifier which will be explained in more detail in Section II-B is also shown in Fig. 4. In contrast to the auxiliary amplifier, the carrier amplifier offers an almost constant current consumption and is therefore active even at low input power. Given the fact that the auxiliary amplifier's turn-on point must match the carrier amplifier's input referred 1 dB compression point, determining the amplifier's layout parasitics reliably is essential. Especially the resistive parasitics of the transistors $T_{1,2}$ have to be carefully designed, as parasitics at the emitter of the common-emitter transistors $T_{1,2}$ degenerate the amplifier. Furthermore, the layout realization of the base contact has to be designed for a resistance as low as possible to maintain the transistor's speed. The circuit's input impedance has been designed to match 100 Ω when turned on. The design of the amplifier's output matching network, on the other hand, is based on a different design goal. Considering the amplifiers output impedance when the amplifier is turned off, as shown in Fig. 5, an output impedance of $Z_{\text{out,1}}$ of $10 - j400\ \Omega$ can be observed. As the Doherty amplifier's load modulation is based on the fact that the auxiliary amplifier acts as a high impedance when inactive, a separate matching network consisting of the transmission line $TL_{\text{M,out}}$ is necessary to create a high-impedance behavior. The transmission line transforms the $Z_{\text{out,1}}$ into a $Z_{\text{out,2}}$, increasing the real part of the impedance from 20 Ω to 400 Ω.

B. CARRIER AMPLIFIER

The carrier amplifier is realized as a differential common-emitter stage, followed by a stacked common base stage as shown in Fig. 6. By using a current mirror, the core current

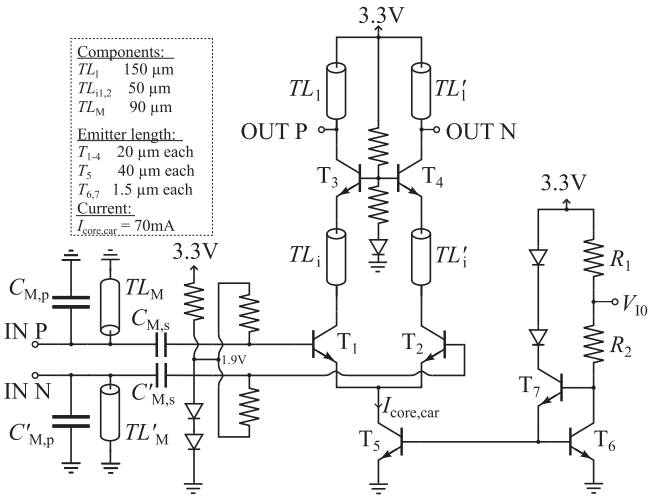

FIGURE 6. Schematic of the proposed carrier amplifier. It consists of a differential cascode amplifier. The core current $I_{\text{core,car}}$ of 70 mA is adjusted using of a current mirror with an emitter follower buffer.

$I_{\text{core,car}}$ is adjusted. It incorporates an emitter-follower buffer to reduce the current mirror's gain error for high mirror ratios due to non-negligible base currents. The carrier amplifier's core current $I_{\text{core,car}}$ amounts to 70 mA. Each of the core transistors T_{1-4} consists of five parallel blocks of $4\times$ 0.96 μm × 0.12 μm to achieve maximum f_T for the chosen current $I_{\text{core,car}}$. To match the amplifier's input to 100 Ω, a parallel shorted stub TL_M with a length of 100 μm and a parallel 20

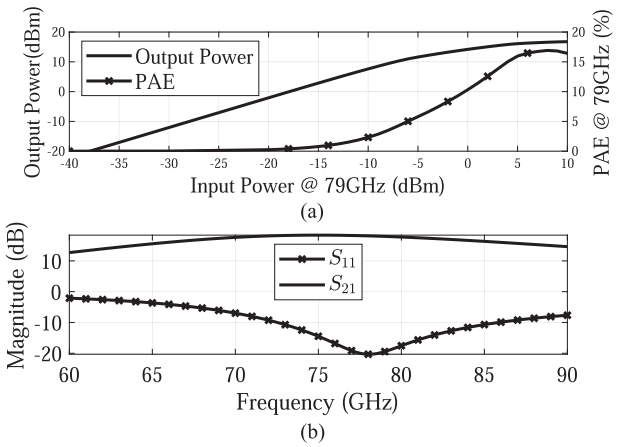

FIGURE 7. (a) Simulated output power and PAE of the proposed carrier amplifier depicted over input power. The amplifier offers a simulated linear power gain of 19 dB and a peak PAE of 16.7%. (b) Simulated input match and small signal power gain versus the operating frequency. The circuit is optimized for 79 GHz after parasitic RC extraction and offers an input matching better than −10 dB from 72 GHz to 85 GHz. In this bandwidth, the small signal gain amounts to at least 17 dB.

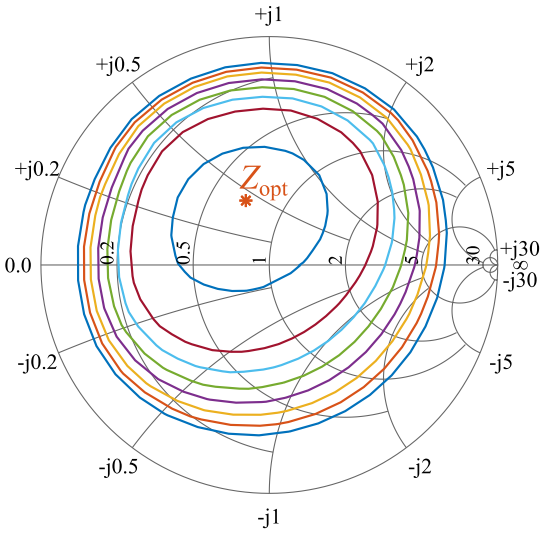

FIGURE 8. Load-Pull simulation of the proposed differential carrier amplifier depicted in a Smith chart that is normalized to 100 Ω. The optimum differential impedance Z_{opt} amounts to 70 Ω + j39 Ω, while the matching network at the carrier amplifier's output is included in the simulation.

fF-MIM capacitor $C_{M,p}$ have been used. The series capacitor $C_{M,s}$ functions as a DC block, and with a size of 180 fF, it has a marginal impact on the input match. According to simulation results, the loss of the input matching network amounts to 0.5 dB. As can be seen in Fig. 7, an input match better than −14 dB was achieved for the frequency region of interest from 76 GHz to 81 GHz, including layout parasitics of the core transistors.

A load-pull analysis of the amplifier's output was performed to maximize the efficiency of the sole carrier amplifier. The corresponding simulation results are shown in Fig. 8. The maximum performance is achieved for an output impedance of $70 + j37\ \Omega$. Therefore a matching network consisting of a series MIM capacitor with a value of 550 fF and 150 μm series transmission line has been designed. The simulated large signal response is given in Fig. 7(a)) and shows an input-referred 1 dB compression point of −4.9 dBm, at which an output power of 11.5 dBm is achieved. While the maximum PAE amounts to 16.7%, the efficiency degrades to 4.1% at 6 dB-PBO. This simulation takes layout parasitics of the core transistors T_{1-4} and EM simulations of the required matching networks into account. For the PAE simulation the power dissipation of the amplifier including the biasing networks is considered.

Besides being integrated into the Doherty circuitry, this carrier amplifier also suits as a reference amplifier for comparison reasons, as it performs comparably to the state-of-the-art [15], [16], [17].

C. LOAD MODULATION

Modulating the output impedance seen by the carrier amplifier is the fundamental mechanism of the Doherty amplifier. Therefore realizing the connection between the carrier and auxiliary amplifier is essential to generate the load-modulating network. In recent publications, this connection is realized with EM simulated couplers [11], [18], [19]. The most common solution at low frequencies is a transmission-line-based quarter-wavelength transformer. For 5 G/LTE frequencies, it can be realized on the PCB level. However, for frequencies around 79 GHz, a quarter-wavelength transmission line amounts to 480 μm in length, which is suitable for on-chip integration. Besides the compact design, a transmission-line-based realization offers the benefit of post-production trimming the length of the transmission line using laser fuses. Thereby the performance can be optimized after production. Due to these arguments, the transmission-line-based approach for the load-modulating network was chosen for this work.

The load-modulating network incorporates the quarter-wavelength transmission line TL_{Q2}, which connects the output of the two amplifiers. This transmission line exhibits a length of 480 μm at a width of 8.5 μm to achieve a characteristic impedance $Z_{0,Q2}$ of 50 Ω. TL_{Q2} is used to transform the impedance at node A in Fig. 1 into the impedance $Z_{out,car}$. As the auxiliary amplifier is connected to node A, the impedance at that point and, thereby, $Z_{out,car}$ is input power-dependent. Assuming a low input power, which results in inactivity of the auxiliary amplifier, the output of the auxiliary amplifier ideally offers a high impedance. Thereby the impedance $Z_{out,car}$ is given as:

$$Z_{out,car} = \frac{Z_{0,Q_2}^2}{Z_{0,Q_3}^2} \cdot Z_L \tag{2}$$

As measurement equipment in the W-band is usually calibrated to a single ended 50 Ω reference, the external load impedance Z_L equals 50 Ω. At an operating frequency of 79

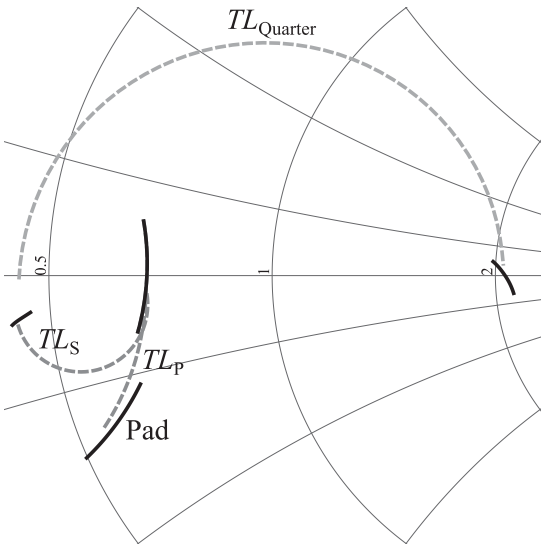

FIGURE 9. Contribution of the individual elements of the output matching and impedance inverting network presented in a smith chart with a reference impedance of 100 Ω. Due to parallel and series transmission lines TL_P and TL_S, the influence of the connecting pad is resonated and transformed into a differential impedance of 50 Ω. The connected quarter-wavelength transmission line TL_{Quarter} transforms it to 200 Ω. When the auxiliary amplifier contributes current to the load for increasing input power, a modulation of the impedance $Z_{\text{out,car}}$ is caused.

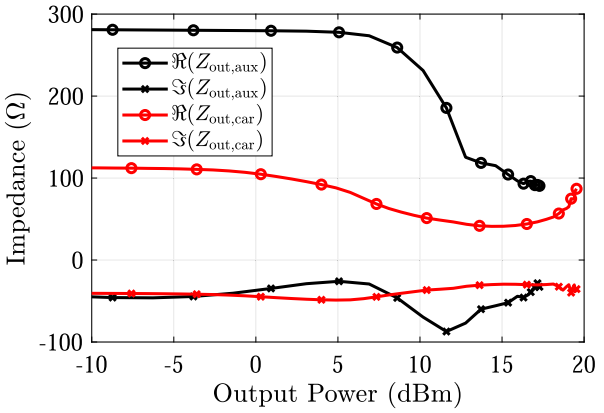

FIGURE 10. Output impedance of the carrier and auxiliary amplifier. For low output powers of the Doherty amplifier, the auxiliary amplifier is inactive, resulting in a real part of the $Z_{\text{out,car}}$ of approximately 100 Ω and a $Z_{\text{out,aux}}$ of 280 Ω. For output powers greater than 0 dBm, $Z_{\text{out,car}}$ reduces due to the load modulation caused by the auxiliary amplifier.

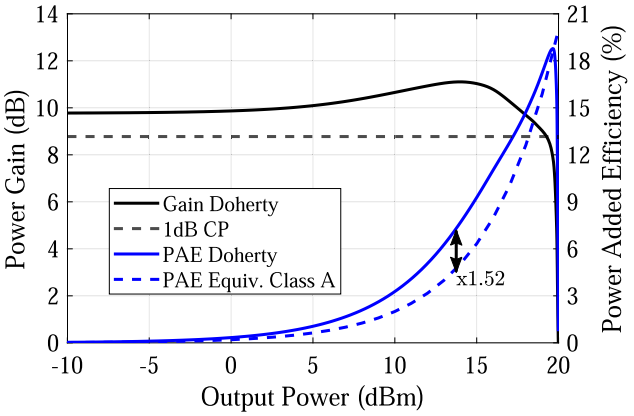

FIGURE 11. Single-tone simulation results of the proposed Doherty amplifier. The solid black line represents the power gain, with the 1 dB compression in the dashed line. A linear power gain of 10 dB can be observed. For an output power above 10 dBm the gain increases as the auxiliary amplifier starts to amplify. The Doherty amplifier achieves a higher PAE than the carrier amplifier, that is scaled to a similar output power.

GHz, Z_L does not amount to precisely 50 Ω due to the capacitance of the connected pad needed to contact the MMIC. As shown in Fig. 9 the output pad result in an impedance of $30 - j12.5$ Ω. Therefore, the impact of the pad has to be minimized by the use of a transmission line in parallel to the pad to form a high impedance parallel resonator with the capacitive behavior of the pad. This results in 50 Ω real part impedance at 79 GHz.

The transmission line TL_{Q3} offers a width of 16 μm to achieve a characteristic impedance of $Z_{0,Q_3} = 35.4\,\Omega$ and transforms Z_L into 25 Ω at node A. As long as the auxiliary amplifier exhibits a high output impedance, TL_{Q3} transforms the impedance into $Z_{\text{out,car}} = 100\ \Omega$.

For increasing input power level, the auxiliary amplifier begins to turn on. Thereby it contributes current to node A, resulting in a reduction of $Z_{\text{out,car}}$, as seen in Fig. 10. It depicts the real part of $Z_{\text{out,car}}$ over the achieved output power. It illustrates that the impedance reduces towards higher output powers as the auxiliary amplifier turns on at an output power of 9 dBm. For low output powers, when the auxiliary amplifier is inactive, $Z_{\text{out,car}}$ remains constant at approximately 80 Ω, which slightly differs from the ideal 100 Ω that would be expected from theory. This is due to the finite output impedance of the auxiliary amplifier in the off-state, as explained in Section II-A.

D. DOHERTY AMPLIFIER - SIMULATION RESULTS

The simulation results of the resulting differential Doherty amplifier are presented in Fig. 11. The solid black line represents the power gain over the achieved output power. The power gain stays constant for small input powers, where only the carrier amplifier is active. In the output power range from 10 dBm to 15 dBm, the gain is increased because the auxiliary amplifier is active and modulates the carrier amplifier's load and extends the 1 dB compression. Considering the PAE, a slight peak in the PAE at an output power of 15 dBm can be observed. Comparing this slightly peaked efficiency to the PAE of the sole carrier amplifier at the PBO, the efficiency is increased by a factor of 1.52 due to the load modulation. In addition, the phase of the transmission along the amplifier for increasing output power, the AM/PM conversion, shows a maximum phase variation of 30° as shown in Fig. 12.

III. MEASUREMENT RESULTS

A. MEASURING FIXTURES

To characterize differential amplifiers, mmWave vector network analyzers (VNA) offer enough ports to characterize

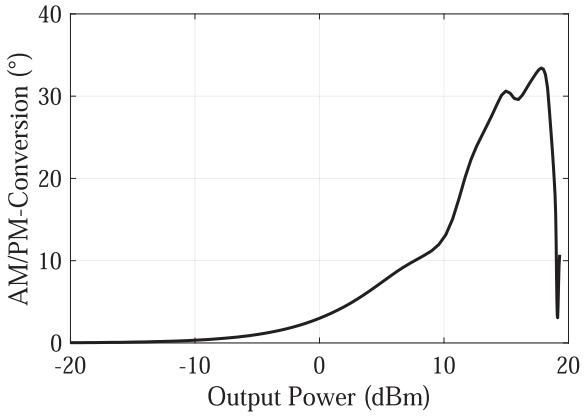

FIGURE 12. Single-tone AM/PM simulation of the proposed Doherty amplifier. While the transmission's phase rises with increasing output power, a slight reduction can be observed at 15 dBm, where the load is modulated by the carrier amplifier.

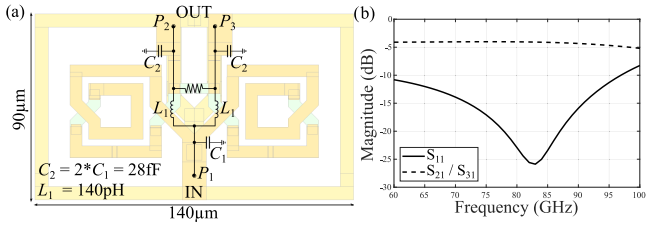

FIGURE 13. (a) Layout of the proposed lumped element Wilkinson divider according to [20] consuming an area of 90 μm × 140 μm. (b) Simulated S-parameters of the Wilkinson divider show an input match better than −10 dB in a frequency range from 60 GHz to 92 GHz. The simulated losses amount to 1.5 dB.

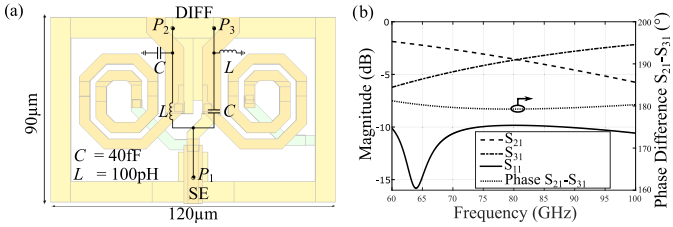

FIGURE 14. (a) Layout of the proposed lumped element balun consuming an area of 90 μm × 120 μm. (b) EM-Simulated, S-parameters of the balun showing an input match better than −10 dB in the frequency region of interest. The losses for the single-ended to differential conversion amount to 0.6 dB.

differential small-signal S-parameters. The available VNA is the E8257D equipped with the 1 mm coaxial frequency extenders N5295 A from Keysight. This setup offers four ports to excite the device under test (DUT) differentially. This VNA is also capable of sweeping the input power to characterize the large signal behavior. However, the VNA cannot be used for the large signal measurements of the proposed structure, as the frequency extenders begin to saturate at an output power of 3 dBm. Given the fact that the proposed amplifier offers medium gain while being highly linear, it cannot be driven into saturation. Therefore the DUT cannot be fully characterized using the available VNA.

Alternatively, a measurement setup using a continuous wave (CW) signal source is used. To measure the amplifier's absolute output power, a power meter with a single ended input has to be connected to the output. Thereby, only one of the two signal pads of the differential output is loaded with 50 Ω. However, to ensure a balanced load at the output of the amplifier, a 50 Ω on-chip resistor is connected via a fuse to the second output pad that is not connected to the power meter. To operate the MMIC fully differentially, the resistor can be removed by laser cutting aluminum fuses after production.

As the CW signal source at the DUT's input is waveguide-based, it can only be connected to one of the signal pads of the differential input. Placing a 50 Ω resistor at the unconnected input pad is not a suitable solution to characterize the differential behavior, as this approach is solely valid for small signal operation. Therefore a lumped element balun forms a single-ended interface towards the amplifier. The realization is shown in Fig. 14. The balun offers a compact layout and exhibits simulated losses below 1 dB in the frequency range of interest. Furthermore, the phase difference between S_{21} and S_{31} remains almost constant at 180° over 30 GHz of bandwidth. Therefore the balun is an excellent choice to differentially drive the input of the power amplifier from a single-ended signal source. The proposed architecture and breakouts of the carrier and the auxiliary amplifier were fabricated in a development lot for IHP's next-generation 0.13 μm SiGe HBT BiCMOS technology SG13G3. The HBTs achieve peak f_T/f_{max} values of about 470 GHz / 650 GHz. Basic features of the HBT technology were outlined in [21], [22]. A micrograph of the fabricated Doherty amplifier and the necessary baluns with overlays of the corresponding schematics is depicted in Fig. 15. The transmission lines that connect the carrier and the auxiliary amplifier are equipped with fuses that can be laser cut. Thus, the line length is adjustable after production. In front of the carrier and the auxiliary amplifier, lumped-element Wilkinson dividers, as presented in Fig. 13 are placed to achieve an equal power split into the amplifiers.

B. SMALL-SIGNAL MEASUREMENTS

The setup to measure the small-signal S-Parameters is depicted in Fig. 16. The VNA is equipped with the 1 mm frequency extender and contacts the MMIC through Cascade Infinity probes in a GSG configuration. To de-embed the probes, a SOLT calibration on an impedance standard substrate was performed to shift the calibration plane towards the probe's tip.

Measurements of the small-signal S-Parameters are presented in Fig. 17. The solid black line represents the input matching, including the input balun, resulting in an S_{11} below −10 dB in the frequency range from 60 GHz to 90 GHz. The small-signal gain amounts to a maximum of 11 dB. However, the bandwidth is reduced, compared to the simulations and the gain maximum is shifted towards lower frequencies. In the frequency range of interest the gain amounts between

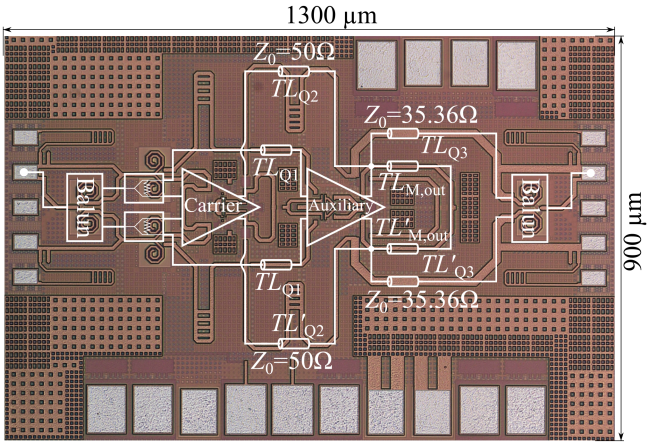

FIGURE 15. Micrograph of the proposed Doherty amplifier, incorporating a lumped element balun at the amplifier's input and output. Furthermore, 50 Ω terminating resistors are placed at the output as an alternative concept to measure the large-signal performance with a single-ended measurement setup. Fuses that can be cut after production are used to choose the output configuration and to adjust the length of the transmission lines inside the amplifier.

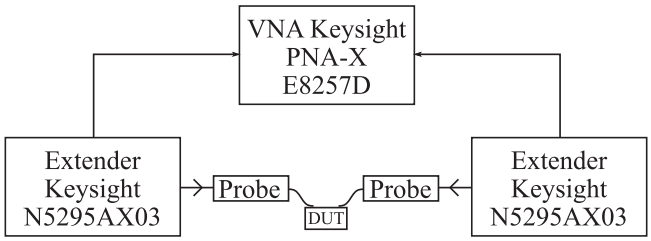

FIGURE 16. Block diagram of the measurement setup for small-signal characterization. The N5295 frequency extenders offer a 1 mm coaxial interface. Therefore, Cascades Infinity Probes are used in a GSG configuration. An SOLT calibration on an impedance standard substrate is performed to shift the calibration plane toward the probe's tip.

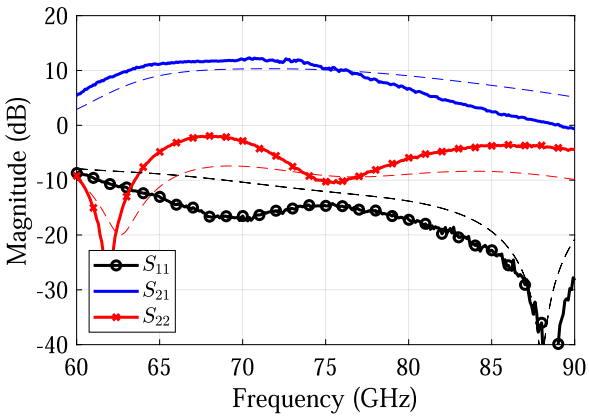

FIGURE 17. S-Parameters of the proposed Doherty amplifier. The results (solid) are shifted towards lower frequencies compared to the simulations (dashed), resulting in a reduced small signal gain in the frequency range of interest. However, below that frequency range, the small signal gain appears higher than simulated.

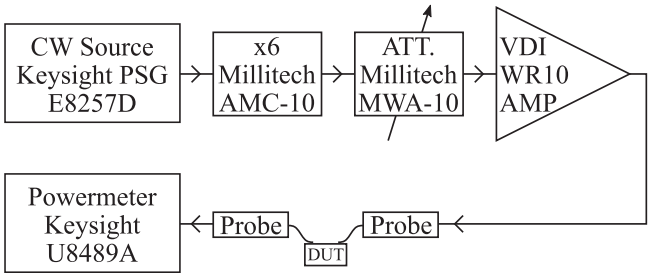

FIGURE 18. Block diagram of the measurement setup for large-signal characterization. A Keysight PSG driving a frequency sixtupler generates a CW signal in the W-band. A cascaded waveguide amplifier with a programmable attenuator ensures enough input power to the DUT to drive it into saturation.

8 dB and 10 dB. A possible reason for that shift towards lower frequencies is the lumped element balun, whose layout parasitics lower its performance.

C. LARGE-SIGNAL SINGLE-TONE MEASUREMENTS

To perform large-signal measurements, the setup shown in Fig. 18 has been used. It consists of a Keysight PSG E8257D to generate a continuous wave signal at a sixth of the desired operating frequency. This signal drives a Millitech AMC-10 frequency sixtupler to generate a CW signal in the W-band. A motorized waveguide attenuator (MWA) by Millitech is used to vary the output power. Between the MWA and the probe that contacts the MMIC's input, a waveguide amplifier (WR10AMP) by Virginia Diodes is used to ensure sufficient power to drive the amplifier. The absolute power level at the amplifier's output is measured with a Keysight 1 mm coaxial power meter (U8489 A). The losses of the fixtures, dominated by the probes and the connected 1 mm coaxial cables, are determined when operating the amplifier with a small input power, where the amplifier operates linearly. By measuring the losses of the 1 mm coaxial cables separately with the VNA, the losses at the input and the output fixture could be separated. Probing a back-to-back structure of contacting pads enabled measuring the losses of the probes. Under the assumption that both probes offer identical losses, the probe losses of 1.5 dB each were de-embedded from the measurement.

The large signal measurement results are presented in Fig. 19 and show the measured power gain and the achieved PAE over the realized output power. In addition to the measured characteristics of the Doherty amplifier the behaviour of the separate breakouts of the carrier and auxiliary amplifier are included. Each circuit was measured independently with the same measurement setup. It can be seen that the power gain of the Doherty amplifer remains constant for low output powers, where the amplifier is operated in the linear regime. At an output power range from 5 dBm to 10 dBm, the power gain slightly increases. Displayed in solid red, it gets clear that the sole carrier amplifier compresses in that range of output power. Due to that fact, the auxiliary amplifier, shown in solid black, offers a power gain greater than 0 dB and modulates the carrier's load. Thereby the auxiliary amplifier increases the

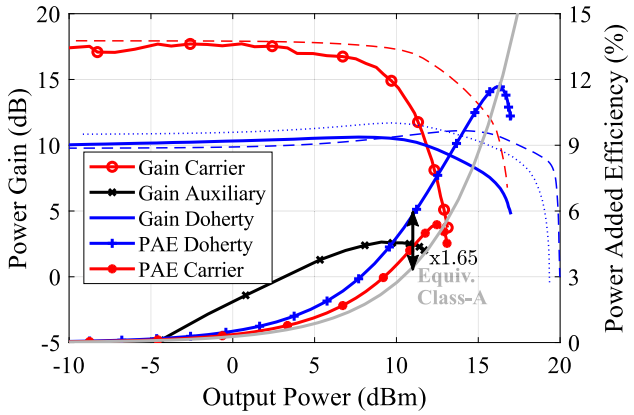

FIGURE 19. Measured large-signal performance of the manufactured carrier, auxiliary, and Doherty amplifier. The solid curves represent the measured power gain over the achieved output power and the corresponding PAEs. Compared to the simulations shown in the dashed lines, it gets clear that the measurement offers approximately 3 dB less saturated output power than simulated. Thereby, the measured efficiencies are lower than shown in the simulation in Section II-D.

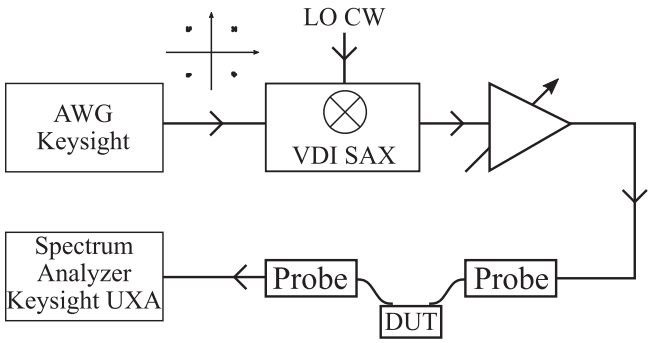

FIGURE 20. Block diagram of the AWG to measure the EVM caused by the amplifier. The modulated input signal configured with the AWG is created at an offset frequency of 1.5 GHz as the following SAX that is operated in block-up-conversion mode has a drastically reduced conversion gain below that offset frequency. Keysight's VSA software is used to evaluate the signal, that is amplified by the DUT, to compute the EVM.

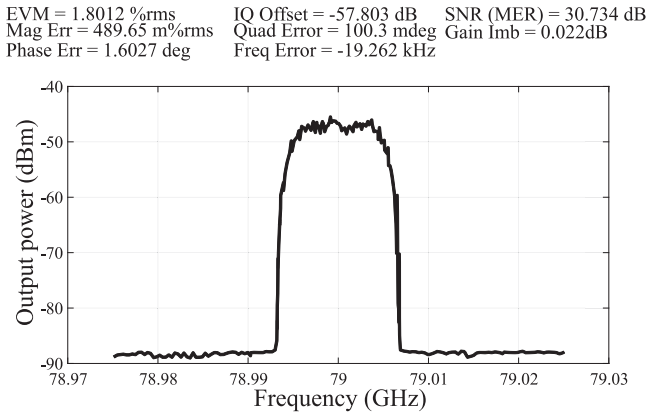

FIGURE 21. Measured output spectrum of the proposed Doherty amplifier for a $10\frac{\text{MSymb}}{\text{s}}$ 64-QAM modulated signal at a carrier frequency of 79 GHz using the measuring setup depicted in Fig. 20. The resulting error vector magnitude amounts to 1.50 %rms while achieving an average output power of 11 dBm.

linear region of operation for the Doherty amplifier. However, when comparing the large signal results to the simulation, a deviation in the output power of approximately 3 dB can be observed. This deviation may be caused by a load impedance that differs from the ideal 100 Ω. To verify this impact, the input impedance of the used power meter has been measured with a VNA. Furthermore, the characteristics of the probe and 1 mm cable, which connects the probe and the power meter, have been measured with the VNA. This results in a measured load impedance for the DUT of $57 + j48$ Ω. Considering this in the simulations, the discrepancy between simulation and measurement reduces by 1 dB (dotted line in Fig. 19), supporting the thesis that the measurement setup causes part of the deviation between simulation and measurement. The cause of the remaining 2 dB deviation cannot be determined entirely. Although EM-simulations of the passive components were taken into account, the realized structures may deviate from the simulations. Especially as the impedance inverting network is tremendiously important in this architecture it is most likely that deviations in the network cause a large part of the remaining deviation between simulation and measurement. Furthermore the realized balun at the input might introduce phase and amplitude imbalances that could impair the differential operation and thereby lower the measured performance. To prove these hypotheses, separate structures of the passive components would be needed. As these were not manufactured these hypotheses can not be proven. However, as the deviation between simulation and measurement can be observed for the Doherty and the sole carrier amplifier, comparing the Doherty and the carrier amplifier still shows that the Doherty amplifier offers superior performance.

D. MODULATION MEASUREMENTS

Besides the single-tone large-signal performance, the large-signal behavior for modulated input signals is investigated separately. Therefore, the setup to measure the EVM of the amplifier for an amplification of a 64-QAM modulated signal is presented in Fig. 20. To generate a modulated signal s_{mod} at 79 GHz, the modulation is first created by Keysight's arbitrary waveform generator (AWG) M8190 A at an intermediate frequency of $f_{\text{IF}} = 1.5$ GHz. s_{mod} feeds a spectrum analyzer extender (SAX) by VDI that is operated in the block up-conversion mode. Thereby s_{mod} is upconverted by a CW local oscillator that also drives the SAX. To compensate for the SAX's conversion loss of approximately 28 dB and to be able to sweep the input power, the waveguide amplifiers VDI WR10AMP and AT-PA-9098 are cascaded with a motorized waveguide attenuator (MWA) and placed at the output port of the SAX. Thus, the EVM can be measured for variable input power to investigate the impact of the amplifier's compression characteristic on the EVM.

The corresponding EVM measurement results are shown in Figs. 21 and 22. Fig. 21 shows the spectrum and the related

TABLE 1. Comparison to State-of-the-Art Automotive SiGe PAs From 76 GHz to 81 GHz

	This work	*This work*	[15]	[16]	[17]	[23]
Technology	130 nm SiGe	130 nm SiGe	130 nm SiGe	120 nm SiGe	130 nm SiGe	90 nm SiGe
Architecture	Doherty	Cascode Amp.	2-stage Cascode Amp.	4-stage CE	Casc. + 2-stage CE	3-stage CE
Supply Voltage(V)	3.3	3.3	2.5	1-2.5	1.7 + 3	1.8
Frequency (GHz)	79	79	77	77	78	80
Power Gain (dB)	9.5	17.1	22.5	17	17.4	20
P_{sat} (dBm)	17.2	13.1	15	17.5	14.2	15.8*
$OP_{1\,\mathrm{dB}}$ (dBm)	13.7	7.5	14*	14.5	11.9	11.2*
Peak PAE	11.6	5.4	7.5	12.8	8	10.7*
PAE @ $OP_{1\,\mathrm{dB}}$ (%)	8.4	3	5*	-	3.9*	-
PAE @ 6 dB PBO (%)	6.1	1.8	2*	-	2*	-
Active Area (mm^2)	0.576	0.12	0.042	0.6	1.2	0.6

* graphically estimated

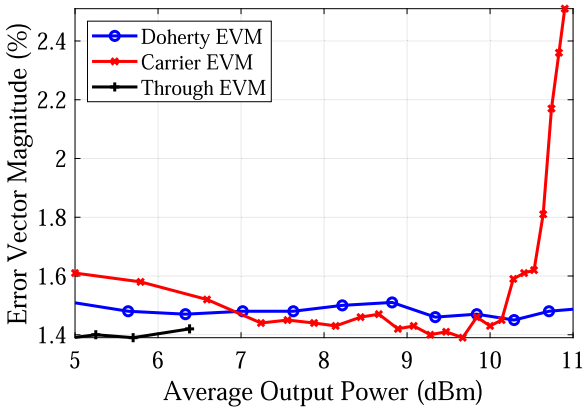

FIGURE 22. Measured error vector magnitude in dependency of the average output power, achieved by the Doherty and the carrier amplifier for a 64-QAM input signal at a symbol rate of 10 $\frac{\mathrm{MSymb}}{\mathrm{s}}$. As the amplifier operates linearly for the given output power range the EVM remains below −17 dB for output powers greater than −5 dBm. For lower output powers, the detected power level is insufficient to measure the EVM reliably. However, the EVM of the carrier amplifier offers a higher EVM for high output powers where the carrier amplifier is operated in saturation.

EVM of the amplifier's output signal for a quadrature amplitude modulation (QAM) with 64 symbols. The symbol rate was set to 10 $\frac{\mathrm{MSymb}}{\mathrm{s}}$, as it offered maximum average power at the signal source's output. The shown spectrum in Fig. 21, was measured at the output of the Doherty amplifier. This measurement verifies the measurement setup, as a modulated bandwidth of 10 MHz can be observed. For this setup, the EVM amounts to only 1.8% RMS at an average output power $P_{\mathrm{avg,out}} = 11$ dBm.

The sweep over the average input power was performed for three DUTs. The first DUT was an on-chip through to evaluate the amount of error caused by the measurement setup, consisting of the input source and the connecting 1 mm cables, and the contacting probes. Fig. 22 displays the EVM of the on-chip through and offers an EVM of 1.4%. Furthermore, the measured EVM of the proposed Doherty amplifier and the reference carrier amplifier are shown. It can be seen that the amplifier slightly increases the EVM to approximately 1.5%, while achieving an average output power of 11 dBm. As measured in the single-tone large signal measurement, the Doherty amplifier still operates linearly up to this output power. Thereby the Doherty amplifier could achieve an even higher $P_{\mathrm{avg,out}}$ during the EVM measurement, but due to the high losses in the measurement setup, the maximum average input power that the signal source can deliver, limits $P_{\mathrm{avg,out}}$ to 11 dBm. As already measured in the single tone large signal scenario, the carrier amplifier is driven into saturation at an output power of 11 dBm, which is also reflected in the measured EVM, displayed in Fig. 22. Up to an average output power $P_{\mathrm{avg,out}}$ of approximately 10 dBm the carrier amplifier offers a low EVM comparable to and even slightly lower than the EVM of the Doherty amplifier. For higher $P_{\mathrm{avg,out}}$, the EVM strongly increases up to 2.5% while the EVM of the Doherty amplifier remains constantly low at 1.5%. This measurement proves that a conventional amplifier represented by the state-of-the-art carrier amplifier can be embedded into a Doherty amplifier to increase the maximum achievable output power while shifting the gain compression towards higher output powers. The higher modulation bandwidths utilized in the application were not achievable with the available measurement setup. However, the shown results highlight the desired improvement due to the Doherty architecture, that is not expected to decrease dramatically with increasing modulation bandwidth.

E. STATE OF THE ART

As shown in Sections III-C and III-D, the proposed Doherty amplifier offers improved performance compared to the embedded, sole carrier amplifier. Compared to the state of the art, which i shown in Table 1, the measured carrier amplifier reaches decent power gain. In contrast saturated output power and power-added efficiency lag behind state-of-the-art amplifiers. However, integrating our proposed carrier amplifier into the Doherty architecture improves the overall performance significantly. The saturated output power can be increased by approximately 4 dB. Output referred 1 dB-Compression point and peak PAE are also improved, making the proposed Doherty amplifier competitive to the state of the art. Regarding the OFDM-relevant back-off operation, the Doherty amplifier achieves a three times higher efficiency than the presented

state-of-the-art amplifiers. This is partly due to the Doherty amplifier still achieving 53 % of its peak PAE in 6 dB back-off thanks to the combination of the carrier and auxiliary amplifier.

IV. CONCLUSION

In this work, we presented a differential Doherty power amplifier in a SiGe BiCMOS technology for automotive radar applications at 79 GHz. For automotive radar, digital, high PAPR modulation schemes like OFDM are a promising technique to cope with inter-sensor interferences. Using a Doherty amplifier allows for more efficient amplification of high PAPR signals than conventional amplifier topologies.

We present the theoretical and simulative design process and the corresponding challenges to design such an amplifier at frequencies as high as 79 GHz. In small- and large-signal measurements, we have shown that the proposed design methodology can be applied to conventional automotive class-A power amplifiers. When embedded into the Doherty architecture, the resulting performance increases in terms of output power, linearity, and back-off efficiency. Thereby automotive power amplifiers can be adapted to the demands originating from OFDM automotive radar.

ACKNOWLEDGMENT

The authors would like to thank the Leibniz Institute for Innovative Microelectronics and its staff for fabricating the MMICs. Furthermore, we thank Christian Bredendiek, Gunnar Briese, and Lasse Cordes for their valuable support for this work.

REFERENCES

[1] C. Waldschmidt, J. Hasch, and W. Menzel, "Automotive radar – From first efforts to future systems," *IEEE J. Microwaves*, vol. 1, no. 1, pp. 135–148, Jan. 2021.

[2] M. Goppelt, H.-L. Blöcher, and W. Menzel, "Automotive radar–investigation of mutual interference mechanisms," *Adv. Radio Sci.*, vol. 8, pp. 55–60, 2010.

[3] H. J. Ng, "Scalable and fully-integrated multi-band radar sensor platform in SiGe BiCMOS technology," in *Proc. Int. Conf. Microw. Millimeter Wave Technol.*, 2021, pp. 1–3.

[4] J. Schoepfel, S. Kueppers, K. Aufinger, and N. Pohl, "A SiGe transceiver chipset for automotive radar applications using wideband modulation sequences," *Int. J. Microw. Wireless Technol.*, vol. 11, no. 7, pp. 676–685, 2019.

[5] B. Nuss, A. Diewald, J. Schoepfel, D. Martini, N. Pohl, and T. Zwick, "76 GHz OFDM radar demonstrator with real-time processing for automotive applications," in *Proc. IEEE MTT-S Int. Conf. Microw. Intell. Mobility*, 2020, pp. 1–4.

[6] S. H. Han and J. H. Lee, "An overview of peak-to-average power ratio reduction techniques for multicarrier transmission," *IEEE Wireless Commun.*, vol. 12, no. 2, pp. 56–65, Apr. 2005.

[7] F. H. Raab et al., "Power amplifiers and transmitters for RF and microwave," *IEEE Trans. Microw. Theory Techn.*, vol. 50, no. 3, pp. 814–826, Mar. 2002.

[8] H. Chireix, "High power outphasing modulation," *Proc. Inst. Radio Engineers*, vol. 23, no. 11, pp. 1370–1392, 1935.

[9] W. H. Doherty, "A new high efficiency power amplifier for modulated waves," *Proc. Inst. Radio Engineers*, vol. 24, no. 9, pp. 1163–1182, 1936.

[10] R. Pengelly, C. Fager, and M. Ozen, "Doherty's legacy: A history of the Doherty power amplifier from 1936 to the present day," *IEEE Microw. Mag.*, vol. 17, no. 2, pp. 41–58, Feb. 2016.

[11] S. Hu, S. Kousai, and H. Wang, "A broadband mixed-signal CMOS power amplifier with a hybrid class-g Doherty efficiency enhancement technique," *IEEE J. Solid-State Circuits*, vol. 51, no. 3, pp. 598–613, Mar. 2016.

[12] H. T. Nguyen and H. Wang, "A coupler-based differential Doherty power amplifier with built-in baluns for high mm-Wave linear-yet-efficient gbit/s amplifications," in *Proc. IEEE Radio Freq. Integr. Circuits Symp.*, 2019, pp. 195–198.

[13] X. Li et al., "A 110-to-130 GHz SiGe BiCMOS doherty power amplifier with a slotline-based power combiner," *IEEE J. Solid-State Circuits*, vol. 57, no. 12, pp. 3567–3581, Dec. 2022.

[14] J. Schoepfel, H. Rücker, and N. Pohl, "A differential SiGe HBT doherty power amplifier for automotive radar at 79 GHz," in *Proc. IEEE 23rd Topical Meeting Silicon Monolithic Integr. Circuits RF Syst.*, 2023, pp. 44–46.

[15] V. Giammello, E. Ragonese, and G. Palmisano, "A 15 SiGe BiCMOS PA for 77 automotive radar," *IEEE Trans. Microw. Theory Techn.*, vol. 59, no. 11, pp. 2910–2918, Nov. 2011.

[16] A. Komijani and A. Hajimiri, "A wideband 77, 17.5 fully integrated power amplifier in silicon," *IEEE J. Solid-State Circuits*, vol. 41, no. 8, pp. 1749–1756, Aug. 2006.

[17] H. Li, J. Chen, D. Hou, S. Peng, and W. Hong, "A w-band power amplifier with LC balun in 0.13 μm SiGe BiCMOS process," in *Proc. IEEE Int. Symp. Radio-Freq. Integr. Technol.*, 2017, pp. 202–204.

[18] H. T. Nguyen and H. Wang, "A coupler-based differential mm-Wave Doherty power amplifier with impedance inverting and scaling baluns," *IEEE J. Solid-State Circuits*, vol. 55, no. 5, pp. 1212–1223, May 2020.

[19] E. Kaymaksut, D. Zhao, and P. Reynaert, "Transformer-based Doherty power amplifiers for mm-Wave applications in 40 CMOS," *IEEE Trans. Microw. Theory Techn.*, vol. 63, no. 4, pp. 1186–1192, Apr. 2015.

[20] N. Pohl, T. Jaeschke, and K. Aufinger, "An ultra-wideband 80 GHz FMCW radar system using a SiGe bipolar transceiver chip stabilized by a fractional-n PLL synthesizer," *IEEE Trans. Microw. Theory Techn.*, vol. 60, no. 3, pp. 757–765, Mar. 2012.

[21] H. Rücker and B. Heinemann, "Device architectures for high-speed SiGe HBTs," in *Proc. IEEE BiCMOS Compound Semicond. Integr. Circuits Technol. Symp.*, 2019, pp. 1–7.

[22] B. Heinemann et al., "SiGe HBT with ft/fmax of 505 GHz/720 GHz," in *Proc. IEEE Int. Electron Devices Meeting*, 2016, pp. 3.1.1–3.1.4.

[23] H.-C. Lin and G. M. Rebeiz, "A 70–80 SiGe amplifier with peak output power of 27.3 dBm," *IEEE Trans. Microw. Theory Techn.*, vol. 64, no. 7, pp. 2039–2049, Jul. 2016.

JAN SCHOEPFEL (Member, IEEE) received the B.Sc., M.Sc., and Dr.-Ing. degrees in electrical engineering and information technology from Ruhr University Bochum, Bochum, Germany, in 2014 and 2016, respectively. Since 2017, he has been with the Institute for Integrated Systems, Ruhr University Bochum. His current research interests include the concepts and integrated circuits for radar sensors for fully autonomous driving. He was the co-recipient of the EuMIC 2021 Best Student Paper Award.

TOBIAS T. BRAUN (Graduate Student Member, IEEE) was born in Düsseldorf, Germany, in 1996. He received the B.Sc. and M.Sc. degrees in electrical engineering and information technology from Technical University (TU) Dortmund, Dortmund, Germany, in 2016 and 2019, respectively. He is currently working toward the Ph.D. degree with the Institute of Integrated Systems, Ruhr University Bochum, Bochum, Germany. Since 2019, he has been a Research Assistant with the Institute of Integrated Systems, Ruhr University Bochum. His current research interests include integrated circuit and system design for automotive applications. He was the recipient of the European Microwave Integrated Circuit Conference (EuMIC) Young Engineer Prize from European Microwave Week in 2021.

JULIA HELLWIG received the B.Sc. degree in electrical engineering and information technology from Ruhr University Bochum, Bochum, Germany, in 2022. Currently, she completes the master program electrical engineering and information technology with the Ruhr University Bochum. Her main research focuses on electronics. Since 2019, she has been a Student Assistant with the Institute of Integrated Systems, Ruhr University Bochum.

HOLGER RÜCKER received the Diploma and Ph.D. degrees in physics from the Humboldt University of Berlin, Berlin, Germany, in 1986 and 1988, respectively. From 1989 to 1991, he was a Staff Member with the Humboldt University Berlin. From 1991 to 1992, he was with the Max Planck Institute for Solid State Research, Stuttgart, Germany. In 1992, he joined Leibniz Institute for High Performance Microelectronics (IHP), Frankfurt (Oder), Germany, where he is engaged in research on physics and fabrication of semiconductor devices. His research interests include SiGe bipolar devices, complementary metal-oxide-semiconductor (CMOS) and BiCMOS process development, and high-frequency characteristics of active and passive devices. He was responsible for the development of IHPs 130-nm SiGe BiCMOS technologies SG13S and SG13G2.

NILS POHL (Senior Member, IEEE) received the Dipl.-Ing. and Dr.-Ing. degrees in electrical engineering from Ruhr University Bochum, Bochum, Germany, in 2005 and 2010, respectively. From 2006 to 2011, he was a Research Assistant with Ruhr University Bochum, where he was involved in integrated circuits for millimeter-wave (mm-wave) radar applications. In 2011, he became an Assistant Professor with Ruhr University Bochum, Bochum, Germany. In 2013, he became the Head of the Department of mm-wave radar and high-frequency sensors with the Fraunhofer Institute for High Frequency Physics and Radar Techniques, Wachtberg, Germany. In 2016, he became a Full Professor of integrated systems with Ruhr University Bochum. He has authored or coauthored more than 200 scientific papers and has issued several patents. His research interests include ultrawideband mm-wave radar, design, and optimization of mm-wave integrated SiGe circuits and system concepts with frequencies up to 300 GHz and above, and frequency synthesis and antennas. He is a Member of VDE, ITG, EUMA, and URSI. He was the recipient of the Karl-Arnold Award of the North Rhine-Westphalian Academy of Sciences, Humanities and the Arts in 2013, and IEEE MTT Outstanding Young Engineer Award in 2018. He was the co-recipient of the 2009 EEEfCom Innovation Award, 2012 EuMIC Prize, 2015 Best Demo Award of the IEEE Radio Wireless Week, Best Paper Award at EUMIC 2012, Best Demo Award at RWW 2015, and Best Student Paper Awards at RadarConf 2020, RWW 2021, and EuMIC 2022.